A graceful break-up: serendipitous self-assembly of a ferromagnetically coupled [Ni^{II}_{14}] wheel

Eleftheria Agapaki,[a] Mukesh K. Singh,[a] Angelos B. Canaj,[a] Gary S. Nichol,[a] Jürgen Schnack*[b] and Euan K. Brechin*[a]

[a]*EaStCHEM School of Chemistry, The University of Edinburgh, David Brewster Road, Edinburgh, EH9 3FJ, Scotland, UK. Email: ebrechin@ed.ac.uk .*

[b]*Universitat Bielefeld, Postfach 100131, D-33501 Bielefeld, Germany. Email: jschnack@uni-bielefeld.de*

Abstract

The complex [$Ni^{II}_{14}(HL^2)_{12}(HCOO)_{14}Cl_{14}$] describes an aesthetically pleasing wheel displaying ferromagnetic nearest neighbour exchange.

Introduction

Interest in the magnetic properties of polymetallic clusters of Ni^{II} began with the development of magneto-structural correlations of [Ni_2] dimers[1] and [Ni_4] cubanes[2] that revealed a dependence of the sign and magnitude of the exchange interaction on both the Ni-X-Ni bridging angle and the anisotropy of the Ni^{II} ion.[3] The large axial zero-field splitting displayed by the latter in certain geometries also lends itself to the construction of both single-molecule magnets (SMMs)[4] and single-ion magnets (SIMs)[5] displaying slow relaxation of the magnetisation. Indeed, recent studies of Ni^{II} SIMs at both ambient and high pressure[6] have revealed how magnetic anisotropy is extremely susceptible to even small structural distortions, in turn highlighting target geometries[7] and directing the synthetic methodologies required to engineer molecules possessing giant magneto-anisotropies.[8]

Flexible N,O-bridging ligands have proved particularly successful in the construction of polymetallic clusters of Ni^{II} displaying a variety of topologies and nuclearities, including supertetrahedra,[9] wheels,[10] planar discs[11] and icosahedra.[12] The pro-ligand (3,5-dimethyl-1H-pyrazol-1-yl)methanol (HL^1) belongs in this family, having been employed to make both mono- and tetranuclear clusters of Ni^{II}.[13] Here, we expand this chemistry to include the synthesis, structure and characterisation of [$Ni_{14}(HL^2)_{12}(HCOO)_{14}Cl_{14}(MeOH)(H_2O)$]·$4Me_2CO$ (**1**·$4Me_2CO$, HL^2 = 3,5-dimethylpyrazole), an aesthetically pleasing wheel formed serendipitously via the in-situ transformation of HL^1 to HL^2.

Results and discussion

The reaction of $NiCl_2·6H_2O$ and HL^1 in a basic MeOH solution heated at 65 °C for 40 minutes affords compound **1** (Fig. 1) upon diffusion of acetone into the cooled mother liquor (see the SI for full experimental details). Crystals of **1** are in a tetragonal crystal system and structure solution was performed in the space group $P4_2/n$ (see the SI for full crystallographic details, Table S1, Fig. S1). The asymmetric unit contains half the formula unit.

The metallic skeleton of **1** is a single stranded [Ni^{II}_{14}] wheel (Fig. 2A). The bridging between each pair of Ni^{II} ions is the same around the entire wheel and consists of one μ-Cl ion (Ni-Cl-Ni, ~82.0-85.1°), and one μ-O atom (Ni-O-Ni, ~102.8-103.2°) and one μ-carboxylate which both derive from the syn, syn, anti-bridging formate (Fig. 2B). The six-coordinate Ni^{II} ions are all in distorted octahedral geometries with their {NiO_3Cl_2N} coordination spheres completed by a terminally bonded HL^2 ligand. The latter and the formate ions originate from the in-situ reaction of HL^1.[14] The only exception to this is Ni5,

{NiO_4Cl_2}, in which there resides a disordered MeOH/H_2O molecule in place of the HL^2 ligand. The wheel is non-planar with nearest neighbour Ni^{II} ions being above and below the plane running through the middle of the fourteen metal ions, i.e., they form a zigzag/sinusoidal "up-down-up-down" motif as the wheel is circumnavigated (Fig. 2C-D). The approximate dimensions of the wheel are, Ni1···Ni1', ~12.7 Å. The terminally bonded MeOH molecules are H-bonded to acetone molecules of crystallisation (O(H)···O, ~2.72 Å). Closest inter-cluster interactions are between neighbouring HL^2 ligands and between HL^2 ligands and the Cl ions (C/N···C/N/Cl > 3.6 Å). In the extended structure the wheels pack in eclipsed columns down the *c*-axis, with the remaining acetone molecules of crystallisation lying in a head-tail fashion in the voids between the wheels (O···C, ~3.6 Å; Fig. S2).

A subsequent investigation of reaction conditions does not reveal any simple relationship between reaction time, temperature and ligand degradation, but did reveal that **1** can be made directly from $NiCl_2{\cdot}6H_2O$, formic acid (or sodium formate) and HL^2, and, perhaps unsurprisingly, in larger yields (see the SI for full details). A search of the Cambridge Structural Database reveals that there are approximately thirty Ni wheels reported, ranging in nuclearity from [Ni_5] to [Ni_{24}].[15] By far the most common are [Ni_6] and [Ni_{12}] wheels,[16] with complex **1** being just the second example of a [Ni_{14}] wheel.[17] The first example is a large (~2 nm diameter) oval-shaped wheel in which neighbouring Ni ions are connected by artificial tripeptides (Ni···Ni, ~8 Å). Compound **1** also represents the first Ni^{II} wheel built with 3,5-dimethylpyrazole (or 1*H*-pyrazole) and indeed is the largest nuclearity Ni cluster known with either ligand.

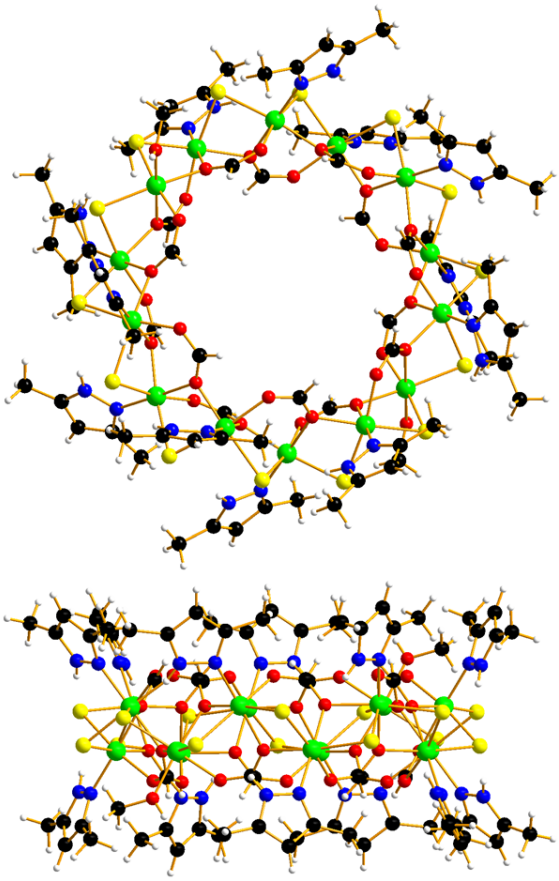

Fig 1. Orthogonal views of the molecular structure of complex **1** viewed perpendicular (top) and parallel to the [Ni_{14}] 'plane'. Colour code: Ni = green, O = red, N = blue, C = black, H = white, Cl = yellow. Acetone molecules of crystallisation are removed for clarity.

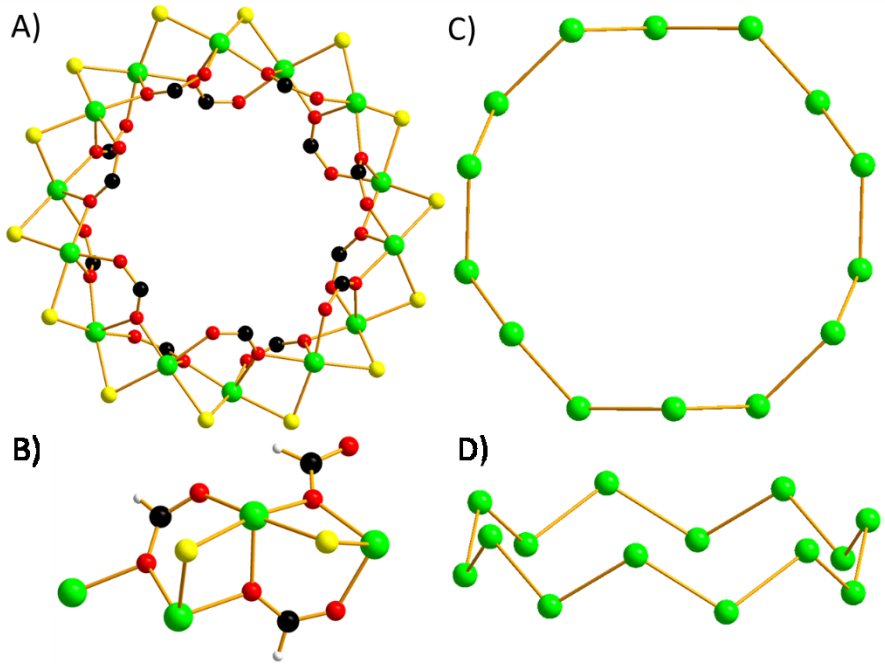

Fig. 2 (A) The magnetic core of **1**. (B) Close-up of the bridging between neighbouring Ni^{II} ions. The metallic core of viewed perpendicular (C) and parallel (D) to the [Ni_{14}] 'plane'. Colour code: Ni = green, O = red, N = blue, C = black, H = white.

Dc magnetic susceptibility (χ) and magnetisation (M) measurements of **1** were taken in the T = 300-1.80 K, B = 0.1 T and T = 2.0-10 K and B = 0.5-9.0 T temperature and field ranges, respectively. These are plotted as the χT product versus T, and M versus B in Fig. 3. The T = 300 K value of χT = 18.5 cm^3 K mol^{-1} is equal to the value expected for fourteen non-interacting Ni^{II} ions with g = 2.30. Upon cooling the χT value remains relatively constant, increasing only very slowly to ~24 cm^3 K mol^{-1} at 50 K before rising sharply to a maximum of ~104 cm^3 K mol^{-1} at T = 3 K. The value then drops to ~96.3 cm^3 K mol^{-1} at 2 K. The M vs B data increases rapidly with increasing field, saturating at a value of M = 32.1 μ_B at T = 2 K and B = 9 T. The susceptibility and magnetisation data are therefore indicative of weak ferromagnetic nearest neighbour exchange and the stabilisation of an S = 14 spin ground state.

The magnetic susceptibility data can be simulated using exact diagonalisation[18] and an isotropic spin-Hamiltonian $\widehat{H} = -2\sum_{i<j} J_{ij}\,\hat{\vec{s}}_i \cdot \hat{\vec{s}}_j$ with a coupling scheme that assumes just one independent exchange interaction between nearest neighbours, J = + 4 cm^{-1} with g = 2.30 (Fig. 3, black curve). The addition of a next nearest neighbour interaction makes no difference to the quality of the simulation. Given that this interaction is computed to be very weak and ferromagnetic by DFT (*vide infra*) this is to be expected. The DFT calculated values for the seven crystallographically unique interactions also simulate the susceptibility well if they are scaled by a factor of 1.4 (Fig. 3, red curve). This simple isotropic model, however, does not explain the low temperature magnetisation data, which requires inclusion of the single ion anisotropy of the Ni ions, D(Ni), to be included $\widehat{H} = D\sum_i \left(\hat{\vec{s}}_i \cdot \vec{e}_i\right)^2$, where $\vec{e}_i = \vec{e}_i(\vartheta_i, \varphi_i)$ is the direction of the local easy axis. Computational limitations direct us toward employing a [Ni_7] wheel, with the results multiplied by two to mimic the [Ni_{14}] wheel. The magnetisation data is simulated nicely with J = +4 cm^{-1} and D(Ni) = -5 cm^{-1} with the anisotropy axes tilted from the axis of the wheel by ϑ = 30°, $\varphi_i = 2\pi i/7$, in agreement with *ab initio* NEVPT2 calculations (see Figure 3, blue curves, and below). The magenta curves in Fig. 3 demonstrate for the isotropic case that the substituted [Ni_7] model system is close to the original except for low

temperatures where the *S* = 14 ground state cannot be reproduced. The ferromagnetic exchange in **1** is consistent with magneto-structural correlations developed for halide-bridged Ni^{II} dimers where the sign and magnitude of the interaction is dictated by the Ni-Cl-Ni angle – with a switch from antiferromagnetic to ferromagnetic occurring at approximately ≤102° and increasing with decreasing angle.[19] Note the Ni-Cl-Ni angles in **1** are ~82-85°.

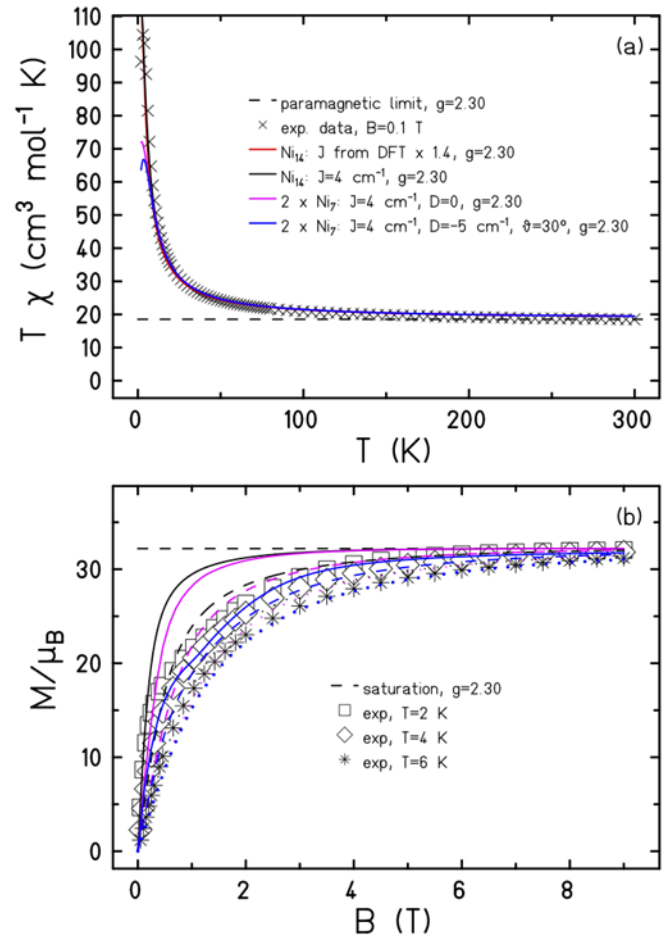

Fig. 3 (a) Magnetic susceptibility data potted as the χT product versus *T* measured in a field, *B* = 0.1 T between *T* = 300-2.0 K. (b) *M* vs *B* data in fields *B* = 0.5 – 9 T and temperature range *T* = 1.8 - 10 K. The curves are simulations of the experimental data (solid, dashed, dotted in (b) for the three temperatures). See the main text for details.

To further understand the origin and sign of the magnetic coupling constants we have performed DFT calculations on models created from **1** (**1A-C**, Fig. S3, Tables S1-S3). All seven unique exchange interactions are in the range $+1.7 \leq J \leq +3.9$ cm^{-1}, consistent with the experimental values. The narrow range of values obtained can be attributed to the presence of similar structural parameters for each metal ion, with the relatively small Ni-μ-O/Cl-Ni angles resulting in ferromagnetic exchange (Table S4).[19] To further explore the origin of the sign and magnitude of these interactions we have performed overlap integral calculations[20-22] between the singly occupied molecular orbitals (SOMOs) of the Ni^{II} ions in a bimetallic model (**1D**) created from **1** (Fig. S4). These calculations suggest competition between one moderate interaction [$<Ni(\alpha)d_{x^2-y^2}||Ni(\beta)d_{z^2}>$] and three weak interactions [$<Ni(\alpha)d_{x^2-y^2}||Ni(\beta)d_{x^2-y^2}>$; $<Ni(\alpha)d_{z^2}||Ni(\beta)d_{x^2-y^2}>$, $<Ni(\alpha)d_{z^2}||Ni(\beta)d_{z^2}>$]. The former contributes to the antiferromagnetic and the latter to the ferromagnetic part of the exchange. In this case, the three weak interactions dominate and the overall result is the observation of a weak ferromagnetic

interaction. Spin density analysis suggests a strong spin delocalisation mechanism, with the spin densities on the Ni^{II} ions being between 1.668-1.682. Of the three different bridging moieties, the Cl ion has the largest spin density (0.122 - 0.141; Fig. S5). To further investigate the contribution from the μ-Cl ion to the total magnetic exchange, we have replaced it with a point charge in model **1D**. This results in an antiferromagnetic interaction, changing from +2.3 cm^{-1} to -6.2 cm^{-1}, clearly suggesting the major ferromagnetic contribution to the exchange comes from the μ-Cl ion. Bearing in mind the connectivity of next-nearest neighbour Ni^{II} centres through a formate group, we have also estimated the next-nearest neighbour magnetic exchange interaction using model **1E** (Fig. S6). This is estimated to be very small and ferromagnetic, J = + 0.5 cm^{-1} . All the Ni^{II} ions in **1** possess slightly distorted octahedral geometries (Table S5) and are therefore expected to have axial zero-field splitting parameters of the order $D \leq$ -10 cm^{-1}. *Ab initio* NEVPT2 calculations performed using ORCA[23] reveals values of the $D \leq$ -6.5 cm^{-1}, with the major contribution arising from the $d_{xy} \rightarrow d_{x^2-y^2}$ electronic transition (Fig. S7, Tables S6-12).[24] The D(Ni) axes are oriented approximately along the N(pyrazole)-Ni-O and O(MeOH)-Ni-O vectors, tilted at angles of ϑ = ~32-37° from the axis of the wheel.

In summary, the *in-situ* transformation of HL^1 to HL^2 and concurrent formation of formate anions results in the self-assembly of an aesthetically pleasing [Ni_{14}] wheel, with subsequent examination of reaction conditions leading to a more 'rational' synthetic procedure. Magnetic measurements reveal weak, ferromagnetic exchange interactions, with the susceptibility data simulated with a single exchange constant, J = + 4 cm^{-1}. The DFT computed values also simulate the data well, albeit they need scaled by a factor of 1.4. The simulation of the magnetisation data requires inclusion of D(Ni) = -5 cm^{-1} tilted at an angle ϑ = 30° with respect to the axis of the wheel. Theoretical calculations are in agreement with experimental observations, revealing the major contribution to the ferromagnetic exchange is mediated through the bridging Cl ions. Attempts to make analogues of compound **1** containing different M^{II} ions and other bridging halides, pseudohalides and carboxylates are underway.

This work was supported by The Leverhulme Trust (RPG-2021-176).

Notes and references

a) A. P. Ginsberg, R. L. Martin, and R. C. Sherwood, *Inorg. Chem*., 1968, **7**, 932-936; b) A. P. Ginsberg, *Inorg. Chim. Acta. Rev*., 1971, **5**, 45-68.

M. A. Halcrow, J.-S. Sun, J. C. Huffman and G. Christou, *Inorg. Chem*., 1995, 34, 4167– 4177.

a) A. Wilson, J. Lawrence, E.-C. Yang, M. Nakano, D. N. Hendrickson and S. Hill, *Phys. Rev. B* 2006, **74**, 140403; b) J. P. S. Walsh, S. Sproules, N. F. Chilton, A. L. Barra, G. A. Timco, D. Collison, E. J. L. McInnes and R. E. P. Winpenny, *Inorg. Chem.,* 2014, **53**, 8464–8472.

J. Miklovič, D. Valigura, R. Boča and J. Titiš, *Dalton Trans.,* 2015, **44**, 12484–12487.

G. Aromí, S. Parsons, W. Wernsdorfer, E. K. Brechin and E. J. L. McInnes, *Chem. Commun*., 2005, 5038-5040.

R. Ruamps, R. Maurice, L. Batchelor, M. Boggio-Pasqua, R. Guillot, A. L. Barra, J. Liu, E.-E. Bendeif, S. Pillet, S. Hill, T. Mallah and N. Guihéry, *J. Am. Chem. Soc.*, 2013, **135**, 3017-3026.

K. E. R. Marriott, L. Bhaskaran, C. Wilson, M. Medarde, S. T. Ochsenbein, S. Hill and M. Murrie, *Chem. Sci.*, 2015, **6**, 6823-6828.

G. A. Craig, A. Sarkar, C. H. Woodall, M. A. Hay, K. E. R. Marriott, K. V. Kamenev, S. A. Moggach, E. K. Brechin, S. Parsons, G. Rajaraman and M. Murrie, *Chem. Sci*., 2018, **9**, 1551-1559.

R. Shaw, I. S. Tidmarsh, R. H. Laye, B. Breeze, M. Helliwell, E. K. Brechin, S. L. Heath, M. Murrie, S. Ochsenbein, H.-U. Güdel and E. J. L. McInnes, *Chem. Commun*., 2004, 1418-1419.

A. J. Blake, C. M. Grant, S. Parsons, J. M. Rawson and R. E. P. Winpenny, *J. Chem. Soc., Chem. Commun*., 1994, 2363-2364.

S. T. Meally, G. Karotsis, E.K. Brechin, G. S. Papaefstathiou, P. W. Dunne, P. McArdle and L. F. Jones, *CrystEngComm*., 2010,12, 59-63.

D. Geng, X. Han, Y. Bi, Y. Qin, Q. Li, L. Huang, K. Zhou, L. Song and Z. Zheng, *Chem. Sci*., 2018, **9**, 8535-8541.

a) V. M. Leovac, R. Petković, A. Kovács, G. Pokol and K. M. Szécsény, *J. Therm. Anal. Cal*., 2007, **89**, 267; b) R. Touzani, M. Haibach, A. J. Nawara-Hultzsch, S. El Kadiri, T. J. Emge and A. S. Goldman, *Polyhedron*, 2011, **30**, 2530; c) J. Lim, G. Kim, K. Do, S. Lee, S. Ryu, D. Yoshioka and M. Mikuriya, *X-ray Struct. Anal. Online*, 2015, **31**, 49; d) A. Mar, S. J. Retting, A. Storr and J. Trott, *Can. J. Chem*., 1988, **66**, 101; e) F. Paap, E. Bouwman, W. L. Driessen, R. A. G. de Graaff and J. Reedijk, *J. Chem. Soc. Dalton Trans*., 1985, 737.

W. L. Driessen, *Recl. Trav. Chim*., 1982, **101**, 441-443.

See for example, a) A. H. Mahmoudkhani and V. Langer, *Inorg. Chim. Acta*, 1999, 294, 83-86; b) A. L. Dearden, S. Parsons and R. E. P. Winpenny, *Angew. Chem. Int. Ed*., 2001, **40**, 151-154.

See for example, a) G. E. Lewis and C. S. Kraihanzel, Inorg. Chem., 1983, 22, 2895-2899; b) A. J. Blake, C. M. Grant, S. Parsons, J. M. Rawson and Richard E. P. Winpenny, *J. Chem. Soc., Chem. Commun*., 1994, 2363-2364

R. Miyake, A. Ando, M. Ueno and T. Muraoka, *J. Am. Chem. Soc.*, 2019, **141**, 8675−8679.

(a) K. Bärwinkel, H.-J. Schmidt and J. Schnack, *J. Magn. Magn. Mater*., 2000, **212**, 240–250; (b) R. Schnalle and J. Schnack, *Int. Rev. Phys. Chem*., 2010, **29**, 403–452; (c) T. Glaser, V. Hoeke, K. Gieb, J. Schnack, Chr. Schröder, P. Müller, *Coord. Chem. Rev.*, 2015, **289-290**, 261-278

A. Tamayo, L. Escriche, C. Lodeiro, J. Ribas-Ariño, J. Ribas, B. Covelo and J. Casabó, *Inorg. Chem*., 2006, **45**, 7621-7627.

M. K. Singh, *Dalton Trans.*, 2020, **49**, 4539–4548.

M. K. Singh, A. Etcheverry-Berríos, J. Vallejo, S. Sanz, J. Martínez-Lillo, G. S. Nichol, P. J. Lusby and E. K. Brechin, *Dalton Trans.*, 2022, 51, 8377-8381.

M. K. Singh, N. Yadav and G. Rajaraman, *Chem Commun.,* 2015, **51**, 17732-17735.

F. Neese, *Wiley Interdiscip. Rev. Comput. Mol. Sci*., 2012, **2**, 73–78.

A. Sarkar, S. Dey and G. Rajaraman, *Chem. Eur. J.*, 2020, **26**, 14036-14058.

Supporting Information

Synthetic procedure for compound 1

Method 1

$NiCl_2 \cdot 6H_2O$ (475 mg, 2 mmol), HL^1 (252 mg, 2 mmol) and MeONa (108 mL, 2 mmol) were dissolved in MeOH (10 mL) and refluxed at 65°C for 40 minutes. After filtration and cooling to room temperature, the mother liquor was allowed to slowly diffuse with acetone vapours, affording metallic light blue crystals suitable for X-ray diffraction. Elemental analysis (%) calculated for $Ni_{14}O_{37}N_{32}C_{102}H_{176}Cl_{14}$: C, 32.57 %; H, 4.72 %; N, 11.92 %. Found: C, 32.98 %; H, 5.15 %; N, 12.02 %. Yield $\leq$ 20 %.

Method 2

$NiCl_2 \cdot 6H_2O$ (475 mg, 2 mmol), HL^2 (192 mg, 2 mmol) and NEt_3 (140 µL, 2 mmol) were dissolved in a mixture of MeOH and HCOOH (9:1 ratio, 10 mL) and stirred for 1 hour. After filtration, the mother liquor was allowed to slowly diffuse with acetone, affording metallic light blue crystals suitable for X-ray diffraction. The diffusion can also be successfully performed with Et_2O. Yield ≤ 40 %.

Method 3

$NiCl_2 \cdot 6H_2O$ (475 mg, 2 mmol) and HL^2 (192 mg, 2 mmol) were dissolved in a mixture of MeOH and HCOOH (9:1 ratio, 10 mL) and stirred for 1 hour. After filtration, the mother liquor was allowed to slowly diffuse with acetone, affording metallic light blue crystals suitable for X-ray diffraction. The diffusion can also be successfully performed with Et_2O. Yield ≤ 35 %.

Method 4

$NiCl_2 \cdot 6H_2O$ (475 mg, 2 mmol), HL^2 (192 mg, 2 mmol) and HCOONa (136 mg, 2 mmol) were dissolved in MeOH (15 mL) and stirred for 1 hour. After filtration, the mother liquor was allowed to slowly diffuse with acetone, affording metallic light blue crystals suitable for X-ray diffraction. The diffusion can also be successfully performed with Et_2O. Yield ≤ 40 %.

X-ray crystallography

A suitable crystal of **1** with dimensions 0.85 × 0.12 × 0.09 mm^3 was selected and mounted on a Rigaku Oxford Diffraction SuperNova diffractometer. The crystal was kept at a steady T = 120.15 K during data collection. The structure was solved with the ShelXT solution program using iterative methods and by using Olex2 as the graphical interface. The model was refined with ShelXL using full matrix least squares minimisation on F^2. Full details are provided in Table S1.[1-3] Powder XRD measurements were collected on freshly prepared samples of **1** using a Bruker D2 PHASER with nickel filtered Cu radiation at power 30 kW and current 10 mA. Diffraction patterns were measured from 2θ = 5° - 30°, step size 0.0101°.

Magnetic Measurements

Variable-temperature, solid-state direct current (dc) magnetic susceptibility data down to T = 1.8 K and in fields up to B = 9 T were collected on a Quantum Design PPMS Dynacool. The crystalline sample was embedded in eicosane in a gelatine capsule. Diamagnetic corrections were applied to the observed paramagnetic susceptibility.

Computational Details

Density Functional Theory (DFT) has been used to compute the magnetic exchange coupling constants on three model complexes (models **1A-C**, Figure S3) created from **1** in the Gaussian 09 suite[4] of programs. We have employed the hybrid B3LYP functional[5] together with the TZVP basis set for the Ni, Zn, Cl, O and N atoms and the SVP basis set for the C and H atoms.[6] Model **1A** is a tetra-metallic model in which the two terminal Ni^{II} ions have been replaced with two Zn^{II} ions. The latter is employed to replicate the electronic environment at the Ni^{II} centres. Models **1B-C** are pentametallic containing three Ni^{II} ions and two terminal Zn^{II} ions. To estimate the magnetic exchange coupling constants we have used Noodleman's broken symmetry approach.[7] Spin configurations used to estimate the magnetic exchange coupling constants for models **1A-C** are summarized in Table S2-3. We have employed ORCA software (version ORCA 4.0) to estimate the zero-field splitting parameters for each Ni^{II} centre. This is based on a trimetallic Zn-Ni-Zn model created from **1**.[8] The zeroth-order regular approximation (ZORA) method, together with the ZORA contracted version of the basis set (ZORA-def2-TZVPP for Ni, Zn and ZORA-def-TZVP for rest of the atoms) has been used for the resolution of identity (RI) approximation.[9] For each Ni^{II} centre during state-average complete active space self-consistent field (SA-CASSCF) calculations, we have considered eight electrons in five d-orbitals (CAS (8 electrons/5 3d-orbitals)) in the active space. Ten triplet and fifteen singlet roots are considered during CASSCF calculations. To estimate the zero-field splitting parameter accurately and consider the dynamic correlation we have performed 2^{nd} order N-electron valence perturbation theory.[10] We have used integration Grid 6 for Cl, Ni and Zn, and Grid 5 for the remaining atoms.

Table 1. Crystallographic details for compound **1**.

Compound	**1**
Formula	$C_{87}H_{140}Cl_{14}N_{24}Ni_{14}O_{34}$
$D_{calc.}$/ g cm^{-3}	1.359
μ/mm^{-1}	1.841
Formula Weight	3384.46
Colour	metallic light blue
Shape	rect. prism-shaped
Size/mm^3	0.85×0.12×0.09
T/K	120.15
Crystal System	tetragonal
Space Group	$P4_2/n$
a/Å	37.1760(2)
b/Å	37.1760(2)
c/Å	11.96640(10)
α/°	90
β/°	90
γ/°	90
V/Å^3	16538.2(2)
Z	4
Z'	0.5
Wavelength/Å	0.71073
Radiation type	Mo K_α
Θ_{min}/°	3.195
Θ_{max}/°	26.732
Measured Refl's.	152030
Indep't Refl's	17519
Refl's I≥2 σ(I)	15915
R_{int}	0.0499
Parameters	820
Restraints	25
Largest Peak	1.234
Deepest Hole	-0.615
GooF	1.172
wR_2 (all data)	0.1300
wR_2	0.1273
R_1 (all data)	0.0634
R_1	0.0570
CCDC	2169986

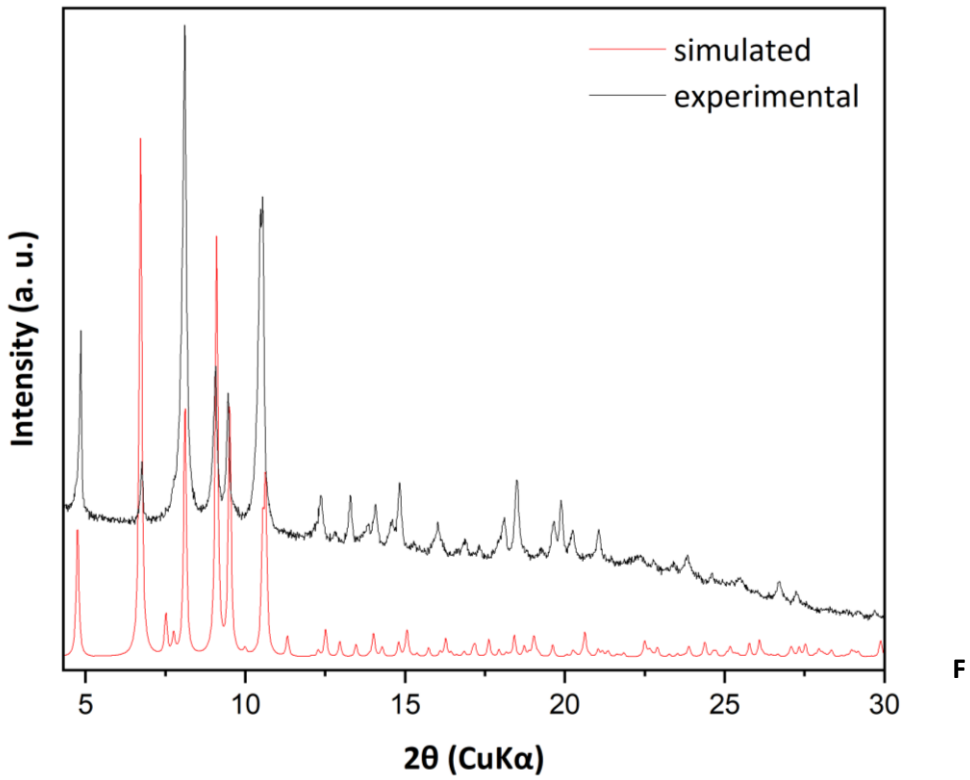

Figure S1. Powder X-ray diffraction of **1**. Experimental data (red) and calculated (black) data.

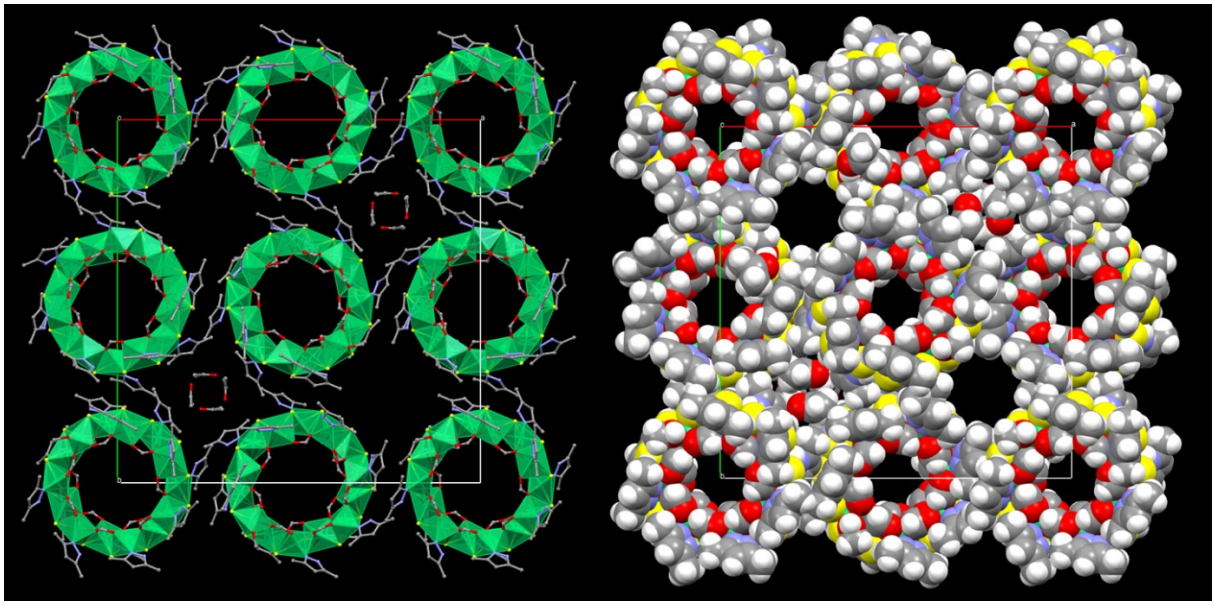

Figure S2. The extended structure of **1** viewed down the *c*-axis of the cell in (left) polyhedral, and (right) space-filling representation. Colour code: Ni = green, O = red, N = blue, C = black, H = white, Cl = yellow.

Table S2. Spin configurations used for model **1A**. Red arrows represent spin-up and blue arrows spin-down.

	***S* value**	**Ni1**	**Ni2**	**Ni3**	**Ni4**
HS	**4**				
BS-1	**2**				
BS-2	**2**				
BS-3	**2**				
BS-4	**2**				
BS-5	**0**				
BS-6	**0**				

Table S3. Spin configurations used for models **1B-C**. Red arrows represent spin-up and blue arrows spin-down.

	***S* value**	**Ni1**	**Ni2**	**Ni3**
HS	**3**			
BS-1	**1**			
BS-2	**1**			
BS-3	**1**			

Table S4. Pertinent structural parameters for **1** alongside the seven calculated magnetic exchange interactions, *J*.

	Avg. Ni-μ_2O/Cl distance (Å)	Ni-O-Ni angle (°)	Ni-Cl-Ni angle (°)	Ni-Cl-Ni-O Dihedral (°)	Ni···Ni distance (Å)	*J* (cm^{-1})
Ni1Ni2	2.258	105.3	83.5	17.9	3.272	+1.7
Ni2Ni3	2.249	103.5	83.2	22.3	3.237	+3.5
Ni3Ni4	2.246	102.9	83.4	17.7	3.229	+2.7
Ni4Ni5	2.250	103.1	82.6	22.5	3.228	+3.0
Ni5Ni6	2.237	103.2	83.8	19.3	3.226	+2.5
Ni6Ni7	2.233	102.5	85.1	21.0	3.234	+3.9
Ni7Ni1’	2.252	104.5	83.8	16.9	3.261	+2.1

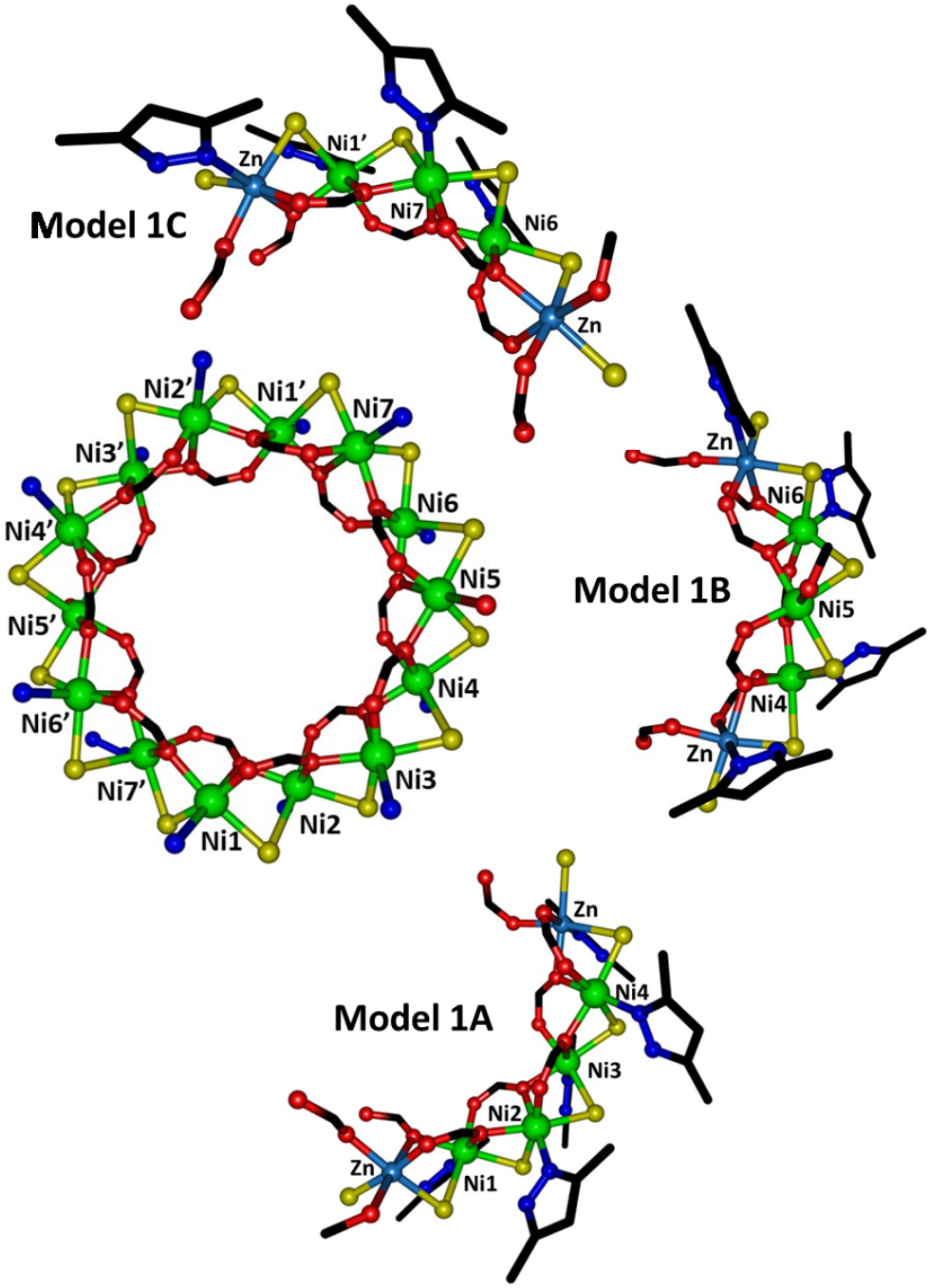

Figure S3. Models **1A-C** on which DFT calculations have been performed in order to estimate the seven magnetic exchange interactions. Colour code: green Ni, light blue Zn, yellow Cl, red O, blue N and black C. H atoms removed for clarity.

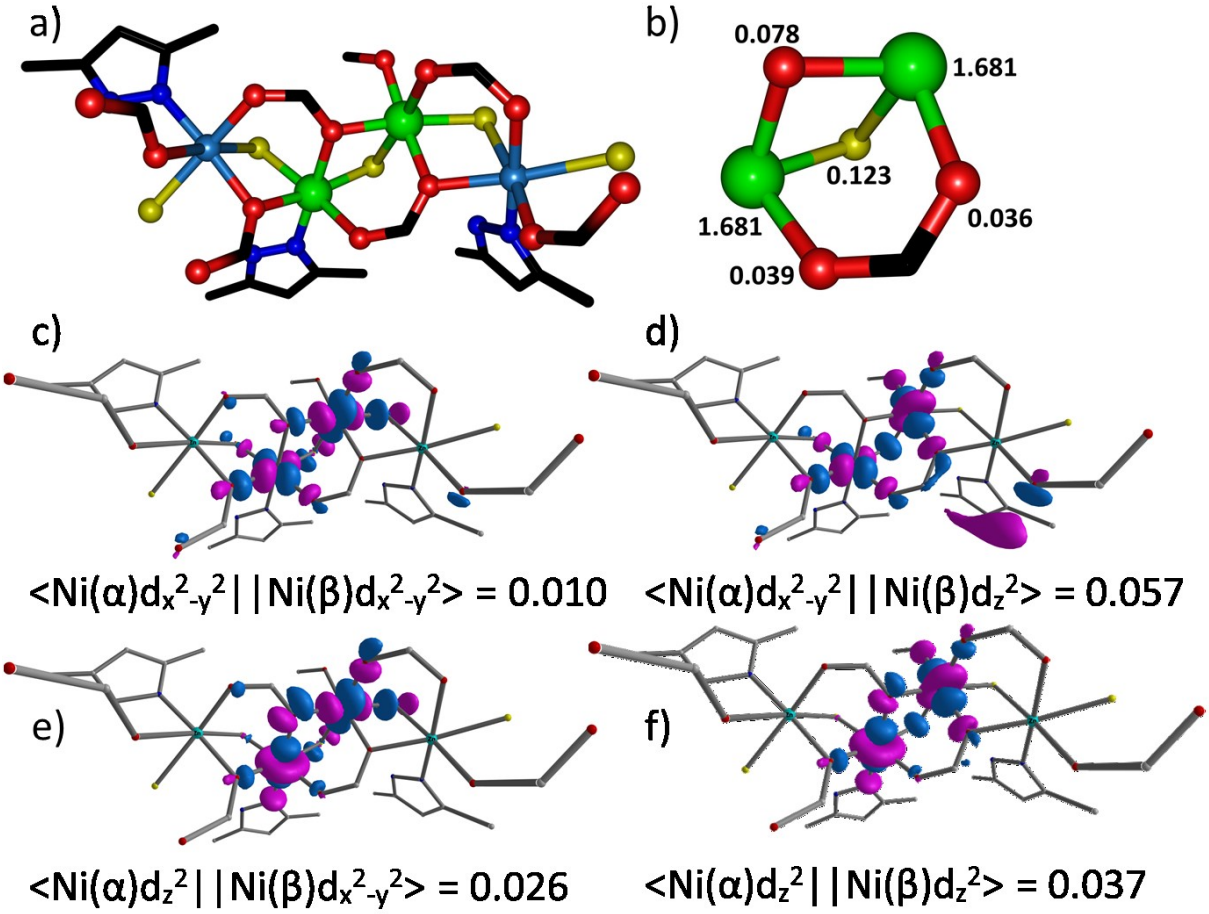

Figure S4. (a) Model **1D** along with (b) DFT computed spin density on important atoms. Colour code is same as Figure S2. (c-f) DFT computed representative overlap integrals figures showing Ni(II) based SOMO(s)-SOMO(s) overlap interactions for **1D**. One moderate $<Ni(\alpha)d_{x^2-y^2}||Ni(\beta)d_{z^2}>$ and three remaining weak interactions result in weak ferromagnetic interaction.

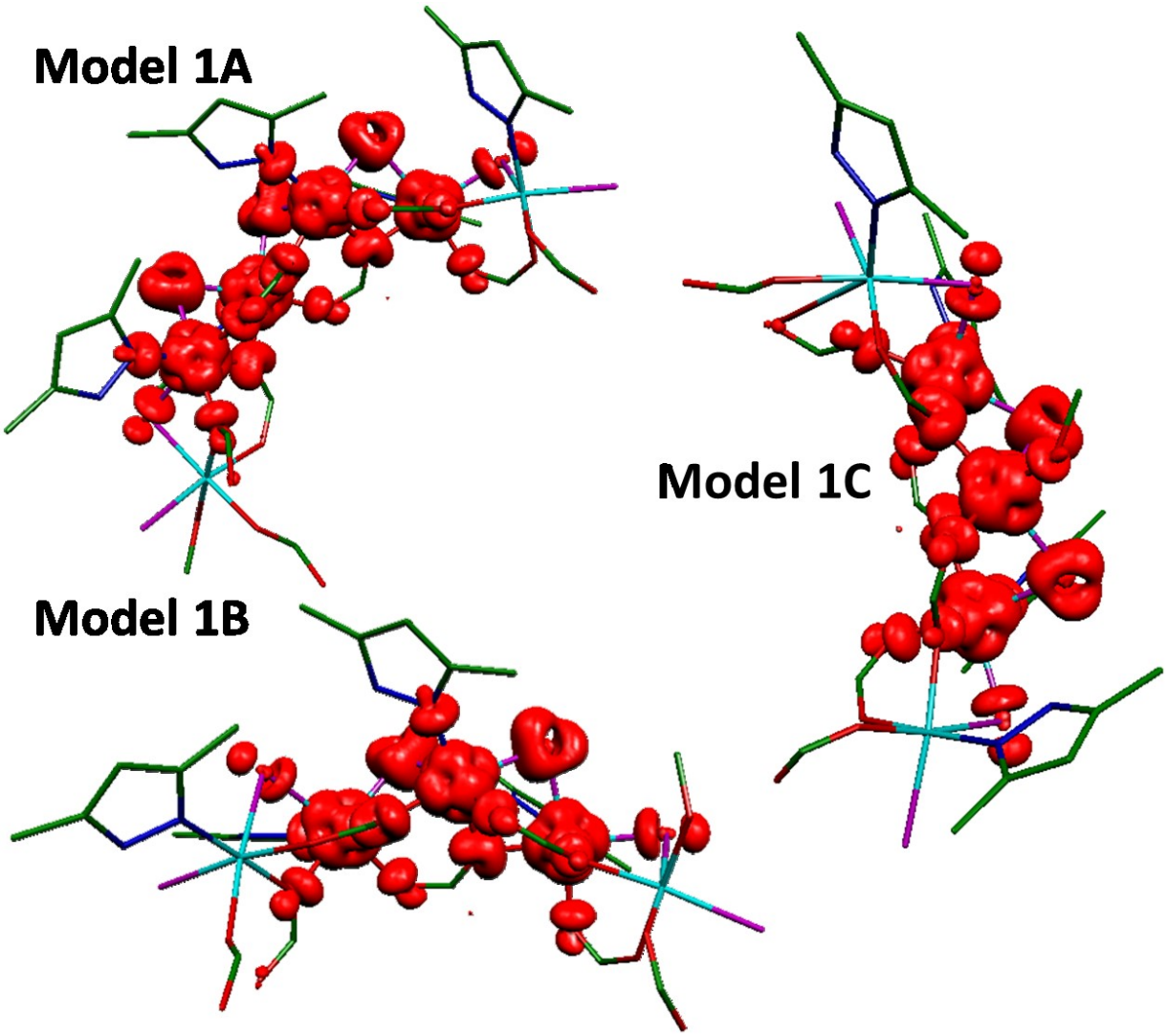

Figure S5. DFT computed spin density plots for Models **1A-C**. The iso-density surface shown corresponds to a value of 0.003 e^{-}/bohr^3. Spin density analysis suggests strong spin delocalisation, with spin densities on the Ni^{II} ions in the range 1.668-1.682. Note that the μ-Cl ions has the largest spin density of the bridging atoms.

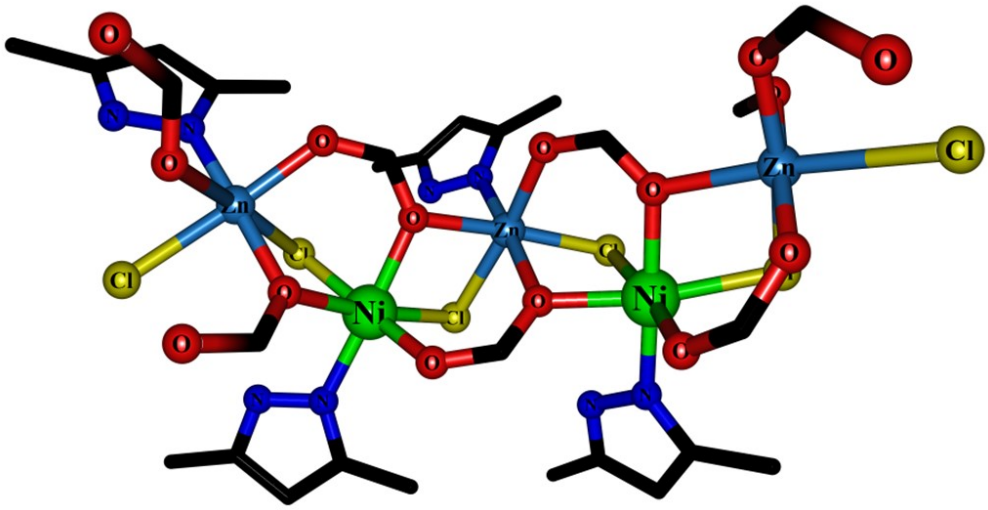
O
Zn
Cl
Ni
O
Zn
Cl
Ni
O
Zn
Cl
O
O
O

Table S6. The NEVPT2 excited states, multiplicity of the states and the transition energies of the ligand field states for Ni1. An electronic transition between the same M_L level magnetic orbitals results in a negative value of *D*, whereas it is positive between different M_L level magnetic orbitals. The relative small magnitude of *D* can be attributed to the large energy separation between the orbitals involved in the transitions. For the first four states the dominant electronic arrangements are $\{(d_{xz})^2(d_{yz})^2(d_{xy})^2(d_{x^2-y^2})^1(d_{z^2})^1\}$, $\{(d_{xz})^2(d_{yz})^2(d_{xy})^1(d_{x^2-y^2})^2(d_{z^2})^1\}$, $\{(d_{xz})^2(d_{yz})^1(d_{xy})^2(d_{x^2-y^2})^2(d_{z^2})^1\}$ and $\{(d_{xz})^1(d_{yz})^2(d_{xy})^2(d_{x^2-y^2})^2(d_{z^2})^1\}$. The major contribution to the negative *D* parameter is coming from the ground to the first excited state electronic transition ($d_{xy} \rightarrow d_{x^2-y^2}$). The electronic transitions from the ground to the second and third excited states ($d_{xz/yz} \rightarrow d_{x^2-y^2}$) contribute to positive *D* values.

D = - 4.9 cm^{-1}; E/D = 0.28 g_{xx}, g_{yy}, g_{zz} (g_{iso}) = 2.233, 2.253, 2.280 (2.255) Energies of d_{xz} (0.0), d_{yz} (168.9), d_{xy} (722.7), $d_{x^2-y^2}$ (7001.9) and d_{z^2} (8745.4) orbitals in cm^{-1}				
NEVPT2 excited states	Multiplicity	NEVPT2 energy levels cm^{-1}	Contribution to *D* cm^{-1}	Contribution to *E* cm^{-1}
0	3	0.0	0.0	0.0
1	3	8135.9	-50.9	0.1
2	3	8914.9	23.2	-23.3
3	3	9708.9	21.1	21.4
4	3	14614.9	0.3	0.1
5	3	15465.4	0.0	0.0
6	1	15674.8	0.0	0.0
7	3	15772.6	0.0	0.0
8	1	15951.6	0.0	0.0
9	1	23575.5	15.0	0.0
10	1	24237.8	-7.2	6.5
11	1	24975.2	-6.9	-6.1
12	3	26218.7	0.0	0.0
13	1	26629.7	0.0	0.0
14	3	26848.8	0.0	0.0
15	3	27293.0	0.0	0.0
16	1	29213.6	0.0	0.0
17	1	30458.6	0.0	0.0
18	1	31047.5	0.0	0.0
19	1	36123.6	0.0	0.0
20	1	36234.9	0.2	0.0
21	1	36631.5	0.1	-0.2
22	1	37073.0	0.2	0.3
23	1	37339.4	-0.7	-0.3
24	1	63581.7	0.0	0.0

Table S7. The NEVPT2 excited states, multiplicity of the states and the transition energies of the ligand field states for Ni2.

D = - 4.7 cm^{-1}; E/D = 0.22 g_{xx}, g_{yy}, g_{zz} (g_{iso})= 2.233, 2.248, 2.276 (2.252) Energies of d_{xz} (0.0), d_{yz} (268.1), d_{xy} (798.0), $d_{x^2-y^2}$ (7258.5) and d_{z^2} (8737.9) orbitals in cm^{-1}				
NEVPT2 excited states	Multiplicity	NEVPT2 energy levels cm^{-1}	Contribution to D cm^{-1}	Contribution to E cm^{-1}
0	3	0.0	0.0	0.0
1	3	8259.5	-50.3	-0.1
2	3	9180.6	22.5	-22.3
3	3	9661.3	21.4	20.9
4	3	14842.5	0.2	0.2
5	3	15479.5	0.0	0.0
6	1	15774.3	0.0	0.0
7	3	15877.0	0.0	0.0
8	1	15928.1	0.0	0.0
9	1	23714.2	15.0	0.0
10	1	24521.5	-7.1	5.0
11	1	24841.4	-7.0	-4.6
12	3	26392.7	0.0	0.0
13	1	26575.0	0.0	0.0
14	3	26944.3	0.0	0.0
15	3	27321.4	0.0	0.0
16	1	29678.3	0.0	0.0
17	1	30129.2	0.0	0.0
18	1	31043.3	0.0	0.0
19	1	36237.3	0.0	0.0
20	1	36320.4	0.4	0.0
21	1	36762.7	-0.7	-0.7
22	1	37252.5	0.9	-0.2
23	1	37486.5	-0.8	0.7
24	1	63667.0	0.0	0.0

Table S8. The NEVPT2 excited states, multiplicity of the states, along with the transition energies of the ligand field states for Ni3.

D = - 6.5 cm^{-1}; E/D = 0.19 g_{xx}, g_{yy}, g_{zz} (g_{iso})= 2.227, 2.243, 2.285 (2.252) Energies of d_{xz} (0.0), d_{yz} (344.1), d_{xy} (931.1), $d_{x^2-y^2}$ (7114.8) and d_{z^2} (9128.9) orbitals in cm^{-1}				
NEVPT2 excited states	Multiplicity	NEVPT2 energy levels cm^{-1}	Contribution to D cm^{-1}	Contribution to E cm^{-1}
Ground state	3	0.0	0.0	0.0
1	3	8014.8	-52.2	0.0
2	3	9363.8	22.5	-21.3
3	3	9799.3	20.8	19.5
4	3	14962.1	0.4	0.4
5	3	15536.6	0.0	0.0
6	1	15602.4	0.0	0.0
7	1	15911.3	0.0	0.0
8	3	16072.3	0.0	0.0
9	1	23490.2	15.3	0.0
10	1	24655.1	-7.1	4.4
11	1	24944.9	-6.9	-4.0
12	3	26323.1	0.0	0.0
13	1	26742.7	0.0	0.0
14	3	27071.2	0.0	0.0
15	3	27558.5	0.0	0.0
16	1	29591.2	0.0	0.0
17	1	30146.1	0.0	0.0
18	1	31434.4	0.0	0.0
19	1	36256.2	0.3	0.0
20	1	36434.3	0.2	0.0
21	1	36832.2	-0.9	-0.9
22	1	37423.9	0.9	-0.1
23	1	37688.1	-0.9	0.8
24	1	63762.7	0.0	0.0

Table S9. The NEVPT2 excited states, multiplicity of the states, along with the transition energies of the ligand field states for Ni4.

D = - 6.5 cm^{-1}; E/D = 0.16 g_{xx}, g_{yy}, g_{zz} (g_{iso})= 2.223, 2.238, 2.279 (2.247) Energies of d_{xz} (0.0), d_{yz} (320.1), d_{xy} (828.9), $d_{x^2-y^2}$ (7279.4) and d_{z^2} (9225.3) orbitals in cm^{-1}				
NEVPT2 excited states	Multiplicity	NEVPT2 energy levels cm^{-1}	Contribution to D cm^{-1}	Contribution to E cm^{-1}
0	3	0.0	0.0	0.0
1	3	8185.6	-50.4	-0.2
2	3	9537.3	21.2	-21.1
3	3	10038.6	20.4	19.8
4	3	15238.7	0.4	0.3
5	1	15621.5	0.0	0.0
6	3	15805.8	0.0	0.0
7	1	15919.3	0.0	0.0
8	3	16379.9	0.0	0.0
9	1	23676.8	15.2	0.0
10	1	24807.9	-7.0	4.5
11	1	25226	-6.8	-4.2
12	3	26597.9	0.0	0.0
13	1	26774.1	0.0	0.0
14	3	27281.3	0.0	0.0
15	3	27794.3	0.0	0.0
16	1	29656	-0.1	-0.1
17	1	30531.5	0.0	0.0
18	1	31439	0.0	0.0
19	1	36610.7	0.2	0.0
20	1	36818.4	0.1	0.0
21	1	37197.4	-0.4	-0.7
22	1	37714	0.4	0.3
23	1	37960.6	-0.7	0.5
24	1	63988.5	0.0	0.0

Table S10. The NEVPT2 excited states, multiplicity of the states, along with the transition energies of the ligand field states for Ni5.

D = - 1.9 cm^{-1}; E/D = 0.00 g_{xx}, g_{yy}, g_{zz} (g_{iso})= 2.250, 2.258, 2.266 (2.258) Energies of d_{xz} (0.0), d_{yz} (500.5), d_{xy} (825.4), $d_{x^2-y^2}$ (7722.2) and d_{z^2} (7972.8) orbitals in cm^{-1}				
NEVPT2 excited states	Multiplicity	NEVPT2 energy levels cm^{-1}	Contribution to D cm^{-1}	Contribution to E cm^{-1}
0	3	0.0	0.0	0.0
1	3	8620.0	-46.3	0.0
2	3	8720.8	24.3	-19.2
3	3	9114.7	24.0	19.8
4	3	14520.6	-0.1	0.0
5	3	14873.2	0.0	0.0
6	3	15413.2	0.0	0.0
7	1	15984.0	0.0	0.0
8	1	16002.3	0.0	0.0
9	1	24146.1	13.7	0.0
10	1	24162.8	-7.3	-0.7
11	1	24325.6	-6.9	0.7
12	3	26358.4	0.0	0.0
13	1	26393.8	0.0	0.0
14	3	26410.4	0.0	0.0
15	3	26911.5	0.0	0.0
16	1	29715.8	0.0	0.0
17	1	29717.9	0.0	0.0
18	1	30611.5	0.0	0.0
19	1	35603.8	0.1	0.1
20	1	36150.6	0.0	0.0
21	1	36154.0	0.3	0.0
22	1	36901.3	-0.9	0.3
23	1	36913.5	-0.9	-0.3
24	1	63435.6	0.0	0.0

Table S11. The NEVPT2 excited states, multiplicity of the states, along with the transition energies of the ligand field states for Ni6.

D = - 4.7 cm^{-1}; E/D = 0.21 g_{xx}, g_{yy}, g_{zz} (g_{iso})= 2.234, 2.247, 2.276 (2.252) Energies of d_{xz} (0.0), d_{yz} (439.3), d_{xy} (784.3), $d_{x^2-y^2}$ (7378.4) and d_{z^2} (8652.7) orbitals in cm^{-1}				
NEVPT2 excited states	Multiplicity	NEVPT2 energy levels cm^{-1}	Contribution to D cm^{-1}	Contribution to E cm^{-1}
0	3	0.0	0.0	0.0
1	3	8250.5	-50.5	0.0
2	3	9216.0	22.8	-22.3
3	3	9630.0	21.4	21.1
4	3	14844.3	0.2	0.2
5	3	15380.3	0.0	0.0
6	1	15829.7	0.0	0.0
7	3	15840.3	0.0	0.0
8	1	15947.6	0.0	0.0
9	1	23732.8	15.0	0.0
10	1	24547.0	-7.1	4.8
11	1	24795.8	-7.0	-4.5
12	3	26402.9	0.0	0.0
13	1	26527.1	0.0	0.0
14	3	26974.5	0.0	0.0
15	3	27148.7	0.0	0.0
16	1	29703.6	0.0	0.0
17	1	30301.6	0.0	0.0
18	1	30743.0	0.0	0.0
19	1	36073.8	0.3	0.0
20	1	36457.1	0.1	0.0
21	1	36662.7	-1.0	-0.9
22	1	37230.7	1.3	0.0
23	1	37354.6	-0.9	0.7
24	1	63622.3	0.0	0.0

Table S12. The NEVPT2 excited states, multiplicity of the states, along with the transition energies of the ligand field states for Ni7.

D = - 5.1 cm^{-1}; E/D = 0.29 g_{xx}, g_{yy}, g_{zz} (g_{iso})= 2.226, 2.248, 2.275 (2.249) Energies of d_{xz} (0.0), d_{yz} (344.3), d_{xy} (824.0), $d_{x^2-y^2}$ (7308.0) and d_{z^2} (9006.2) orbitals in cm^{-1}				
NEVPT2 excited states	Multiplicity	NEVPT2 energy levels cm^{-1}	Contribution to D cm^{-1}	Contribution to E cm^{-1}
0	3	0.0	0.0	0.0
1	3	8289.9	-49.3	0.2
2	3	9140.0	22.0	-22.5
3	3	10003.7	20.6	20.7
4	3	14982.3	0.2	0.1
5	1	15663.7	0.0	0.0
6	3	15665.9	0.0	0.0
7	1	15941.8	0.0	0.0
8	3	16184.0	0.0	0.0
9	1	23755.9	15.0	0.0
10	1	24437.3	-7.1	6.4
11	1	25244.3	-6.8	-6.0
12	3	26441.5	0.0	0.0
13	1	26652.7	0.0	0.0
14	3	27245.6	0.0	0.0
15	3	27476.9	0.0	0.0
16	1	29344.1	0.0	0.0
17	1	30825.0	0.0	0.0
18	1	31022.1	0.0	0.0
19	1	36365.6	0.1	0.0
20	1	36697.4	0.0	0.1
21	1	36946.7	-0.4	-0.3
22	1	37515.7	0.5	0.3
23	1	37717.5	-0.5	-0.2
24	1	63807.0	0.0	0.0

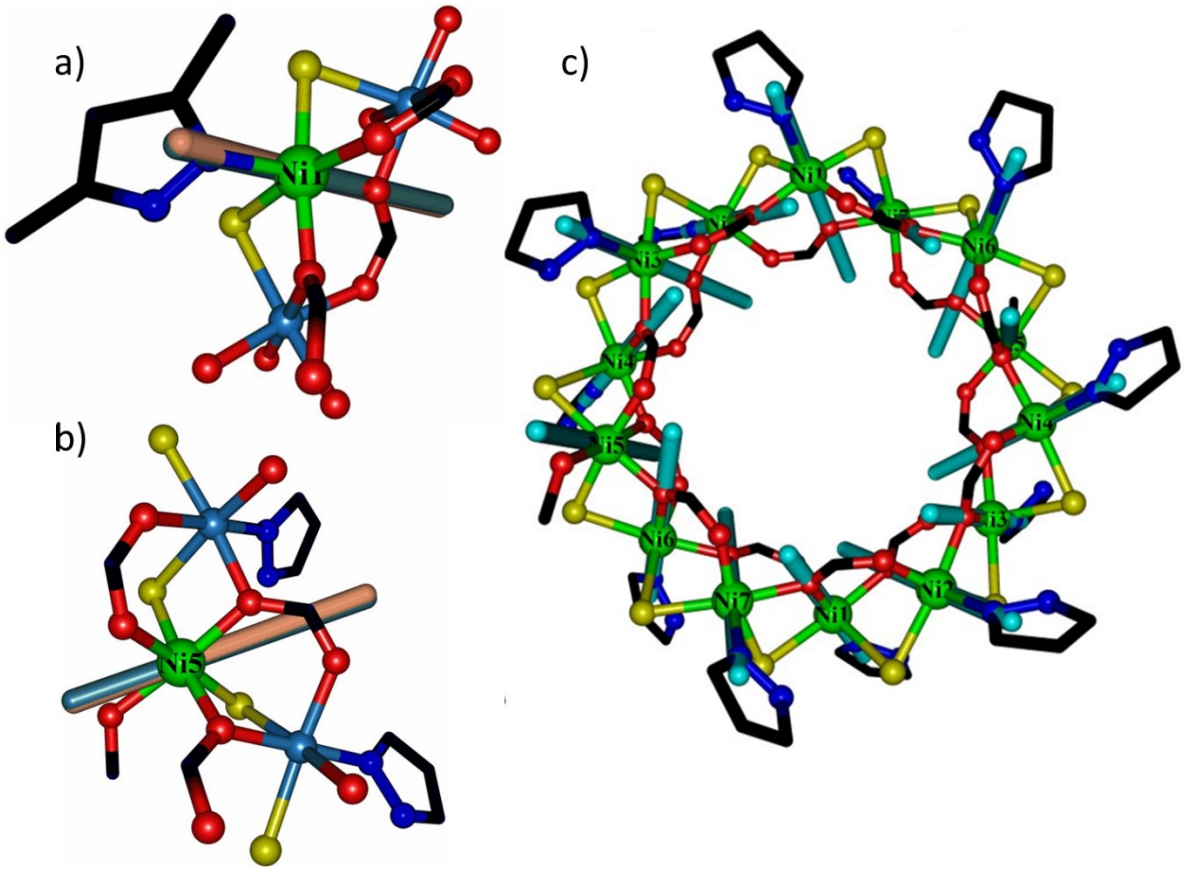

Figure S7. The NEVPT2 computed D_{zz} (cyan coloured bars) and g_{zz} axes (brown coloured bars) for (a) Ni1, (b) Ni5 and (c) **1**. Note that all the Ni^{II} ions have both (coincident) D_{zz} and g_{zz} axes oriented along N atom of HL and an O atom of a formate, with the exception of Ni5 where both axes are slightly tilted away from the donor atoms.

References

1. G. M. Sheldrick, *Acta Cryst.*, 2015, **A71**, 3-8.

2. O. V. Dolomanov, L. J. Bourhis, R. J. Gildea, J. A. K. Howard and H. Puschmann, *J. Appl. Cryst.*, 2009, **42**, 339-341.

3. G. M. Sheldrick, *Acta Cryst.*, 2015, **C71**, 3-8.

4. M. J. Frisch, G. W. Trucks, H. B. Schlegel, G. E. Scuseria, M. A. Robb, J. R. Cheeseman, G. Scalmani, V. Barone, B. Mennucci, G. A. Petersson, H. Nakatsuji, M. Caricato, X. Li, H. P. Hratchian, A. F. Izmaylov, J. Bloino, G. Zheng, J. L. Sonnenberg, M. Hada, M. Ehara, K. Toyota, R. Fukuda, J. Hasegawa, M. Ishida, T. Nakajima, Y. Honda, O. Kitao, H. Nakai, T. Vreven, J. A. Montgomery, Jr., J. E. Peralta, F. Ogliaro, M. Bearpark, J. J. Heyd, E. Brothers, K. N. Kudin, V. N. Staroverov, T. Keith, R. Kobayashi, J. Normand, K. Raghavachari, A. Rendell, J. C. Burant, S. S. Iyengar, J. Tomasi, M. Cossi, N. Rega, J. M. Millam, M. Klene, J. E. Knox, J. B. Cross, V. Bakken, C. Adamo, J. Jaramillo, R. Gomperts, R. E. Stratmann, O. Yazyev, A. J. Austin, R. Cammi, C. Pomelli, J. W. Ochterski, R. L. Martin, K. Morokuma, V. G. Zakrzewski, G. A. Voth, P. Salvador, J. J. Dannenberg, S. Dapprich, A. D. Daniels, O. Farkas, J. B. Foresman, J. V. Ortiz, J. Cioslowski, and D. J. Fox, Gaussian, Inc., Wallingford CT, 2013.

5. (a) A. D. Becke, *Phys. Rev. A*, 1988, **38**, 3098-3101; b) A. D. Becke, *J. Chem. Phys.*, 1993, **98**, 5648; c) C. Lee, W. Yang and R. G. Parr, *Phys. Rev. B: Condens. Matter Mater. Phys.*, 1988, **37**, 785.

6. (a) A. Schäfer, H. Horn and R. Ahlrichs, *J. Chem. Phys.,* 1992, **97**, 2571; (b) A. Schafer, C. Huber and R. Ahlrichs, *J. Chem. Phys.,* 1994, **100**, 5829–5835.

7. L. Noodleman, *J. Chem. Phys.*, 1981, **74**, 5737.

8. F. Neese, *Wiley Interdiscip. Rev. Comput. Mol. Sci.,* 2012, **2**, 73–78.

9. (a) K. Eichkorn, O. Treutler, H. Öhm, M. Häser and R. Ahlrichs, *Chem. Phys. Lett.,* 1995, **242**, 652–660; (b) K. Eichkorn, F. Weigend, O. Treutler and R. Ahlrichs, *Theor. Chem. Acc.,* 1997, **97**, 119–124.

10. (a) C. Angeli, R. Cimiraglia, S. Evangelisti, T. Leininger and J.-P. Malrieu, *J. Chem. Phys.,* 2001, **114**, 10252; (b) C. Angeli, R. Cimiraglia and J.-P. Malrieu, *J. Chem. Phys.*, 2002, **117**, 9138; (c) C. Angeli, R. Cimiraglia and J.-P. Malrieu, *Chem. Phys. Lett.,* 2001, **350**, 297–305.

11. SHAPE, version 2.0; continuous shape measures calculation; Electronic Structure Group, Universiat de Barcelona: Barcelona, Spain, 2010.